Prediction of the fundamental properties of novel Be-B-Ta-based ternary compounds from first-principles calculations

Enamul Haque,[1] Catherine Stampfl [●],[2,*] and M. Anwar Hossain[1]

[1]*Department of Physics, Mawlana Bhashani Science and Technology University, Santosh, Tangail-1902, Bangladesh*
[2]*School of Physics, The University of Sydney, Sydney, New South Wales, 2006, Australia*

Be-B- and B-Ta-based compounds are of great interest for potential technological applications because of their high density and high hardness. However, to date, ternary Be-B-Ta compounds have neither been synthesized nor predicted. In this paper, variable-composition evolutionary crystal structure prediction calculations, based on first-principles calculations, have been performed to determine the stable crystal structures containing Be-B-Ta under ambient conditions. The predicted five compounds BeB_2Ta, BeB_3Ta_2 (high-pressure phase), $BeBTa$, $BeBTa_2$, and Be_2B_2Ta are found to be highly dense and very hard materials. All these compounds are metallic and the effect of spin-orbit coupling (SOC) is significant in them. Two of them (BeB_2Ta and Be_2B_2Ta) are found to be superconductors within Migdal-Eliashberg theory. The calculated critical temperatures, including SOC effects, are 6 and 7 K for BeB_2Ta and Be_2B_2Ta, respectively. Because of their energetic and dynamic stability, these compounds might be favorable to synthesize in the laboratory.

I. INTRODUCTION

Beryllium (Be) and boron (B) are light elements with different electronic structures; Be is metal and B is a semiconductor, while tantalum is an electron-rich transition metal. Beryllium has applications in x-ray equipment [1], as an effective moderator and reflector for neutrons [2], and in aircraft, rockets, etc. [3,4]. However, Be has potential toxicity and is a manufacturing challenge. However, the use of a glove box can make the synthesizing procedure of beryllium-containing compounds safe [5,6]. Different phases are possible by the variation in concentration and combination of Be and B, such as Be_2B [7], Be_4B [8], and the boron-rich compounds BeB_2 [9–13] and BeB_4 (high-pressure phase) [11]. Usually, covalent-bond forming element-based compounds show high hardness, for example, BeB_2 (*Cmcm*) [10], diamond [14], c-BN [15], and BC_2N [16]. Diamond, c-BN, and BC_2N are synthesized under high-pressure and high-temperature conditions [17]. On the other hand, light elements combined with electron-rich transition-metal-based materials also show high hardness [18–22], such as ReB_2 [23], IrN_2 [24], RuO_2 [25], WB_4 [26], and MnB_4 and CrB_4 [27]. This method of combining the light elements with the electron-rich transition metal is very effective to design superhard materials. Different phases of tantalum borides (TaB, TaB_2, Ta_3B_4) have been synthesized at ambient pressure [28], where it has been found that TaB and TaB_2 have high hardness (∼30 GPa) [28–30]. The theoretically calculated Vickers hardness of TaB is 28.6 GPa [31]. Thus, transition-metal-rich borides show good mechanical behavior for practical applications.

Boron-rich BeB_2 and MgB_2 exhibit superconductivity; although the former has a very low transition temperature (0.72 K) [9], the latter has the highest transition temperature (39 K) among simple binary structures [32]. In MgB_2, σ-band electrons strongly interact with in-plane phonons to induce a high superconducting transition temperature. There have been some reports that the boron-rich transition-metal boride TaB_2 exhibits superconductivity with a critical temperature of 9.5 K [33,34], although others report the absence of superconductivity [35,36]. The strong hybridization between the Ta $5d$ and B $2p$ orbitals outside the hexagonal basis plane may be responsible for the absence of superconductivity. Thus, the presence of Be $2s$ states may change the nature of hybridization and give rise to superconductivity. Since BeB_2 ($BeB_{2.75}$) and TaB (TaB_2) exhibit high hardness (28–34 GPa) [28–30], $BeB_{2.75}$ exhibits superconductivity [9] while TaB (TaB_2) does not exhibit superconductivity [35]; therefore, we intend to study what happens in the hardness and superconductivity due to the mixing of Be-B-Ta elements. From the above points of view, it is very interesting to study the possible crystal structures containing Be-B-Ta and their fundamental properties, such as electronic structure and superconducting properties.

In this work, variable-composition evolutionary crystal structure search calculations have been performed to find thermodynamically stable structures containing Be-B-Ta. The predicted BeB_2Ta (monoclinic), BeB_3Ta_2 (body-centered orthorhombic), $BeBTa$ (hexagonal), $BeBTa_2$ (base-centered orthorhombic), and Be_2B_2Ta (body-centered tetragonal), are found to be highly dense and very hard materials. These compounds show metallic band structures and spin-orbit coupling (SOC) effects are significant in them. Boron-rich (BeB_2Ta and Be_2B_2Ta) structures are found to be superconductors within Migdal-Eliashberg theory. Tantalum-rich, or equivalent stoichiometry compounds, do not show superconductivity because of the dominant contribution of Ta $5d$ states.

II. COMPUTATIONAL METHODOLOGY

The thermodynamically stable crystal structure searches for ternary Be-B-Ta were carried out with the first-principles

*catherine.stampfl@sydney.edu.au

evolutionary algorithm implemented in the USPEX code (Universal Structure Predictor: Evolutionary Xtallography) [37–40]. This method of crystal structure search has been successfully applied in many systems (e.g., Refs. [41–44]). The calculation of the lowest-enthalpy phase of a given element composition was performed with the combination of US-PEX and QUANTUM ESPRESSO (for structural relaxation) [45]. At ambient conditions, two separate variable-composition ternary searches were carried out for—three to six atoms per unit cell and—six to 12 atoms per unit cell. When the variable-composition searches were finished, the structure searches at fixed composition predicted to be stable in the previous calculations were carried out with up to 22 atoms per unit cell to find the lowest-enthalpy space group structure for each composition. The atomic relaxation performed during the structure search was performed using the Perdew-Burke-Ernzerhof (PBE) generalized gradient approximation (GGA) [46,47]. For this, Vanderbilt plane-wave pseudopotentials [48], 350-eV cutoff energy for wave function, and 0.8–0.02 Å^{-1} k points for Brillouin zone (BZ) integration, were used. During the variable-composition calculation, USPEX was set to produce 20 generations. Each generation contained 150 individual structures and all structures in the first generation were produced randomly. In all other generations, 20% of the individuals were produced through a random search based on the space group symmetry, 40% of the individuals of one generation were applied to produce individuals of next generations by heredity, 20% of the generated through soft mutations, and 20% of the individuals were produced through transmutation. After the stable structures were obtained, the structural relaxation was performed with a 38-Ry cutoff energy for wave function, 304-Ry cutoff for charge density, and a 0.003–Å^{-1} k-point resolution to calculate formation enthalpy and lattice parameters. The atomic relaxation convergence criteria were set to 1×10^{-8} eV/atom for the energy, and 0.0001 eV/Å for the force on each atom. The best convergence was obtained by using the Thomas-Fermi (TF) charge mixing mode [49]. In all subsequent calculations, these values were kept the same.

By using the strain-stress approach, elastic constants were calculated with the CASTEP code [50]. The same pseudopotentials, functional, cutoff energy, and k points were used in this calculation. The bulk modulus (B) and shear modulus (G) were obtained by using the calculated elastic constants within the Voigt-Reuss-Hill scheme [51]. Chen's formula was used to calculate Vickers hardness [52].

The electronic structure, phonon dispersion, the density of states, and the superconducting transition temperature, T_c, were calculated by using the density funcational perturbation theory (DFPT) as implemented in QUANTUM ESPRESSO. In the electron-phonon coupling (EPC) parameter calculation, the first Brillouin zone (BZ) was sampled using a $4 \times 8 \times 8$, $8 \times 8 \times 8$, $8 \times 8 \times 8$, $8 \times 8 \times 4$, and $8 \times 8 \times 8$ k-point mesh and a $2 \times 4 \times 4$, $4 \times 4 \times 4$, $4 \times 4 \times 4$, $4 \times 4 \times 2$, and $4 \times 4 \times 4$ q-point mesh (for phonons BZ) for BeB_2Ta, BeB_3Ta_2, $BeBTa$, $BeBTa_2$, and Be_2B_2Ta, respectively. Two-times-denser k points were used (for example, $8 \times 16 \times 16$ for BeB_2Ta) for the double delta in the electron-phonon interaction calculation. Besides these parameters, Marzari-Vanderbilt smearing [53] of width 0.03 Ry was used in the
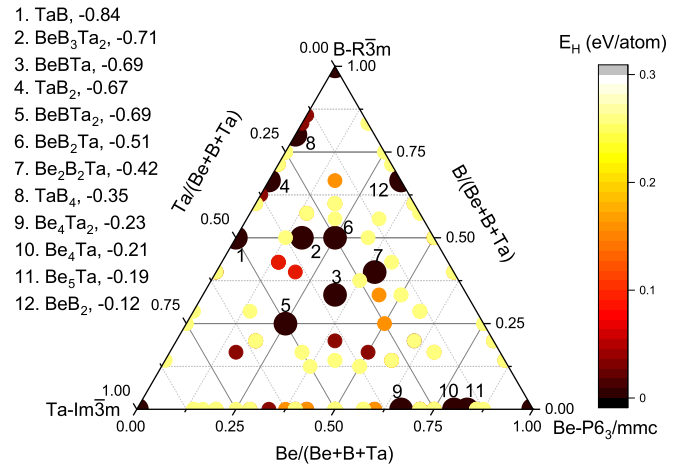

FIG. 1. Ternary convex hull (composition-formation enthalpy) diagram of Be-B-Ta containing compounds at ambient conditions. The left-hand legend shows the chemical formula of all stable structures, with the corresponding formation enthalpy (eV/atom). The right-hand legend represents the value of fitness [i.e., its distance from the convex hull (eV/atom)], with the corresponding colored symbols in the convex hull diagram. The stable phases with lower negative formation enthalpy are indicated by the large circle closer to the convex hull.

BZ sampling. The modified Allen-Dynes equation was used to evaluate T_c with the most widely accepted value of μ^* (0.1) [54]. For the spin-orbit calculation, the fully relativistic pesudopotential of Ta was used [55].

III. RESULTS AND DISCUSSION

A. Structural properties

The ternary crystal structure search (Sec. IV) reveals many possible phases of Be-B, Be-Ta, B-Ta, and Be-B-Ta, as plotted in the ternary convex hull diagram in Fig. 1. The corresponding formation enthalpies [calculated using the equation $\Delta H = E_{tot} - (xE_{Be} + yE_{B} + zE_{Ta})$, where E_{tot} is the total energy of the compound, and E_{Be}, E_{B}, E_{Ta} are the total energy of the corresponding element in its stable phase] of all stable phases are shown in the left legend. The calculated phases of hexagonal beryllium ($P63/mmc$, #194) [56,57], α-rhombohedral boron ($R\bar{3}m$, #160) [58], and body-centered cubic tantalum ($Im\bar{3}m$, #229) [59] are consistent with the available data. Boron-rich BeB_2 ($Cmcm$, #63) is a thermodynamically stable structure, as reported in Refs. [10,13,60]. The present calculations also reproduce the previously reported stable structures TaB ($Cmcm$, #63) [28], TaB_2 ($P6/mmm$, #191) [28], and TaB_4 ($C2/m$, #12) [61]. Besides these phases, the beryllium-rich Be_4Ta_2 ($Imma$, #74), Be_4Ta ($I4/mmm$, #139), and Be_5Ta ($P6/mmm$, #191) are identified for the first time. These phases are thermodynamically stable at ambient conditions. However, several intermediate phases of Be-Ta during solidification reported in Ref. [62] are not found in the present calculations (since it is not usually possible to predict impurity phases [63]). These beryllium-rich phases will not be focused upon in the present paper.

TABLE I. The fully relaxed lattice parameters, space group symbol (number), and the atomic density of the stable ternary compounds containing Be-B-Ta. The fully relaxed atomic coordinates are provided in the Supplemental Material [79].

Compound	Space group	a (Å)	b (Å)	c (Å)	α	β	γ	ρ (g/cm^3)
BeB$_2$Ta	$P2/m(c)$ (#10)	7.2382	3.1629	3.2027	90	90	102.55	9.77
BeB$_3$Ta$_2$	$Imm2$ (#44)	6.5468	3.1666	5.5247	90	90	90	12.98
BeBTa$_2$	$Amm2$(#38)	3.2582	3.3278	8.9107	90	90	90	13.18
BeBTa	$P\bar{6}m2$ (#187)	3.2629	3.2629	3.2404	90	90	120	11.18
Be$_2$B$_2$Ta	$I4/mmm$ (#139)	3.1808	3.1808	8.5602	90	90	90	9.56

The present crystal structure searches that are performed uncover five ternary stable phases containing Be-B-Ta. Among them, BeB$_2$Ta and BeB$_3$Ta$_2$ crystallize in a monoclinic, with unique c axis, and body-centered orthorhombic structure, respectively, while tantalum-rich BeBTa$_2$ forms a base-centered orthorhombic structure.

With 1:1:1 stoichiometry, BeBTa forms a primitive hexagonal structure. Both beryllium- and boron-rich Be$_2$B$_2$Ta crystallize in the body-centered tetragonal structure. The fully relaxed lattice parameters and densities of these phases are listed in Table I. The calculated density of these phases suggest high hardness. The ground-state crystal structures of these compounds are shown in Fig. 2. BeB$_2$Ta forms an AgPtO$_2$-type structure with one B-Ta layer [64].

The orthorhombic BeB$_3$Ta$_2$ forms the NaPd$_3$Si$_2$-type structure [65] while BeBTa forms a hexagonal YbPtP-type structure [66]. Tantalum-rich BeBTa$_2$ is a layered orthorhombic structure, like CeNiC$_2$ [67]. Both beryllium and boron-rich Be$_2$B$_2$Ta are layered tetragonal structures. This is similar to the structure of ThCr$_2$Si$_2$ [68]. The structure of Be$_2$B$_2$Ta consists of a stack of Be$_2$B$_2$ layers. Four Be atoms surround four B atoms. On the other hand, the B atom has four Be

nearest neighbors and one B atom close to it. The combination of them forms a tetragonal pyramid, as shown in Fig. 2(e). In BeB$_2$Ta, BeB$_3$Ta$_2$, and BeBTa$_2$, the B and Ta atoms are bonded together while Be and B are bonded together in BeBTa and Be$_2$B$_2$Ta. To take into account the mechanical stability, the calculated elastic constants of these compounds are listed in Table II. The listed elastic constants fulfill the mechanical stability criteria for these systems described in Ref. [69]. Thus, they are mechanically stable crystal structures. The real phonon frequencies ensure the dynamical stability of a crystal system. The calculated phonon dispersion relations of these compounds, with and without spin-orbit coupling effects, have no negative frequencies, as shown in the left-hand panels of Figs. 6 and 7 (discussed later). Therefore, all these phases are dynamically stable at ambient conditions, and these results suggest that they are favorable to form at ambient conditions. The critical value of Pugh's ratio of 1.75 differentiates brittle and ductile materials [70]. The low value of the ratio for these compounds indicates their brittle nature.

Since these materials are highly dense, it is reasonable to calculate the Vickers hardness by using Chen's formula [52]. This formula gives an estimate of the hardness of a material.
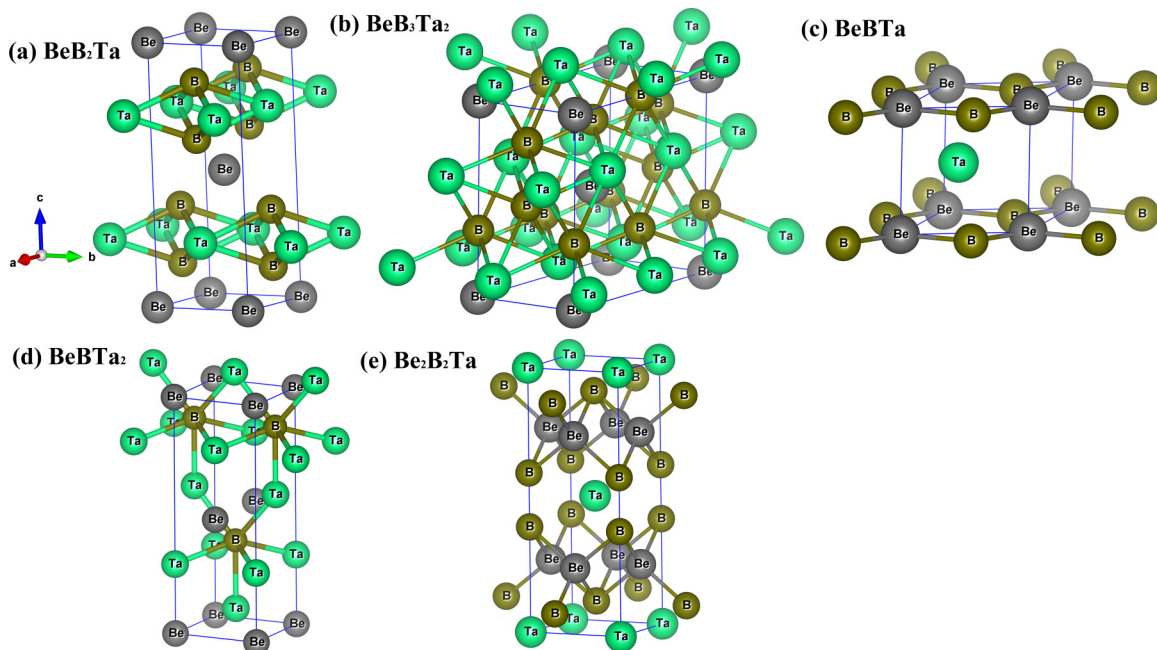

FIG. 2. The ground-state crystal structure of (a) monoclinic (with unique c axis) BeB$_2$Ta, (b) body-centered orthorhombic BeB$_3$Ta$_2$, (c) hexagonal BeBTa, (d) base-centered orthorhombic BeBTa$_2$, and (e) body-centered tetragonal Be$_2$B$_2$Ta.

TABLE II. Calculated elastic constants (c_{ij}), bulk (B) and shear modulus (G) (in GPa), Pugh's ratio (B/G), and theoretical Vickers hardness (H_v) (see the computational methodology in Sec. IV) (GPa) of all stable ternary compounds.

Parameter	BeB$_2$Ta	BeB$_3$Ta$_2$	BeBTa$_2$	BeBTa	Be$_2$B$_2$Ta
c_{11}	489.40	493.03	448.63	491.89	529.43
c_{12}	107.32	146.20	187.01	128.72	116.45
c_{13}	96.97	131.40	127.93	123.49	103.24
c_{15}	−1.81				
c_{22}	554.82	590.28	441.35		
c_{23}	155.52	95.73	115.31		
c_{25}	−0.038				
c_{33}	536.08	596.91	508.54	513.50	543.54
c_{35}	−0.042				
c_{44}	236.31	244.56	199.22		193.92
c_{46}	−1.78				
c_{55}	154.54	238.65	179.01	251.07	
c_{66}	148.02	244.30	244.18		249.46
B	253.34	269.32	250.96	249.83	249.80
G	185.98	231.18	185.03	209.14	211.82
B/G	1.37	1.16	1.35	1.19	1.18
H_v	26.62	37.39	26.68	34.0	34.84

The calculated values of Vickers hardness are presented in Table II. All the phases have very high hardness, with BeB$_3$Ta$_2$ the highest hardness among them. The hardness of BeB$_3$Ta$_2$ is close to the critical value (40 GPa) of a superhard material. Therefore, the calculated hardness suggests that these compounds are potential candidates for superhard materials and applications.

The calculated pressure-dependent formation enthalpy of all stable phases is shown in Fig. 3. All the predicted phases are thermodynamically stable up to the studied pressure range. It is interesting to note that BeB$_3$Ta$_2$ is more favorable to form at 15 GPa than at the ambient condition. Therefore, it can be regarded as a high-pressure phase.

B. Electronic properties

Since the predicted five compounds are stable, we now investigate their electronic structure. The calculated electronic
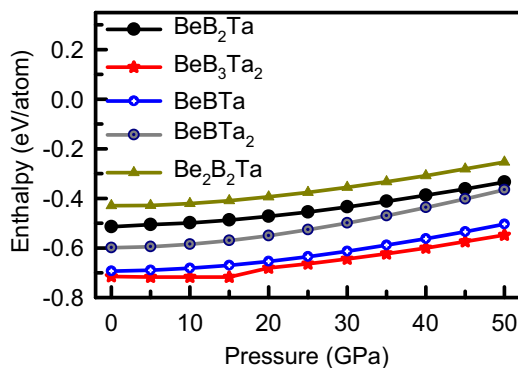

FIG. 3. Pressure-dependent formation enthalpy of the predicted Be-B-Ta containing phases. The negative value of the formation enthalpy indicates that the corresponding phase is thermodynamically stable (or metastable).

band structure, and total and projected density of states of BeB$_2$Ta and BeB$_3$Ta$_2$ are shown in Fig. 4. The gross features of the band structures of these two compounds are completely different, although they contain the same elements. One valence band and one conduction band of BeB$_2$Ta cross the Fermi level. The valence band arises from B $2p$ states, and one conduction band arises from Ta $5d$ states. All these bands are highly dispersive. A pseudogap appears at the X point from B $2p$ states and the Fermi level lies at the middle of the pseudogap. Interestingly, another pseudogap opens up at the C point from dominant Ta $5d$ and minor Be $2p$ states. In that case, the Fermi level lies at the top of the pseudogap.

Although Ta $5d$ states make the dominant contribution to the density of states at the Fermi level, both Be $2p$ and B $2p$ states (especially B $2p$) also make significant contributions. Thus, Ta $5d$ orbitals are strongly hybridized with Be $2p$ and B $2p$, unlike with just B $2p$ orbitals only in TaB$_2$ [35]. This indicates the possibility of superconductivity in BeB$_2$Ta. Only a few bands arisen from Ta $5d$ states are split due to the inclusion of the spin-orbit coupling, as presented by dark pink lines in Fig. 4. The density of states including the spin-orbit coupling effect is not presented here for clarity. Unlike BeB$_2$Ta, six conduction bands of BeB$_3$Ta$_2$ cross the Fermi level, where most of the bands arise from Ta $5d$ states. A pseudogap opens along the T-R directions below the Fermi level from B $2p$ states. From the calculated projected density of states, it is clear that Be $2p$ and B $2p$ states do not make a significant contribution to the density of states at the Fermi level. Furthermore, Ta $5d$ states are strongly hybridized with B $2p$. Therefore, BeB$_3$Ta$_2$ may not be a superconducting material. Like BeB$_2$Ta, certain bands arisen from Ta $5d$ states are split by the effect of spin-orbit coupling, as indicated by dark pink lines. The valence bands and conduction bands overlap in both compounds; hence, they are conductors under ambient conditions.

Unlike the two above-mentioned compounds, only two bands of hexagonal BeBTa arise from Ta $5d$, one crossing the Fermi level and another band only touching the Fermi level at the M point. Neither Be $2p$ nor B $2p$ states make any contribution in the electronic structure around the Fermi level. Three pseudogaps along the Γ-A and L-A directions open due to B $2p$ states. The Fermi level lies at the middle of these pseudogaps. It is clear that the calculated total density of states at the Fermi level is very small and BeBTa can be regarded as a carrier deficient compound. Since it is well known that the PBE functional underestimates the electronic band gap by 30%–100% compared to the experimental value [71,72], this compound may be a semimetal. Note that the band structure of BeBTa has some features of a Weyl semimetal [73]. Further studies are required to clarify these results.

The band structure of tantalum-rich BeBTa$_2$ is significantly different from that of the first three phases. A total of eight bands cross the Fermi level and all these bands arise from Ta $5d$ states. A large pseudogap opens along the Y-A direction. The Fermi level lies at the bottom of the pseudogap. This pseudogap arises from overlapping of the Be $2p$ and B $2p$ states. The density of states at the Fermi level of the Be $2p$ and B $2p$ orbitals is negligibly small compared to that of Ta $5d$ states. Therefore, BeBTa$_2$ may not be a
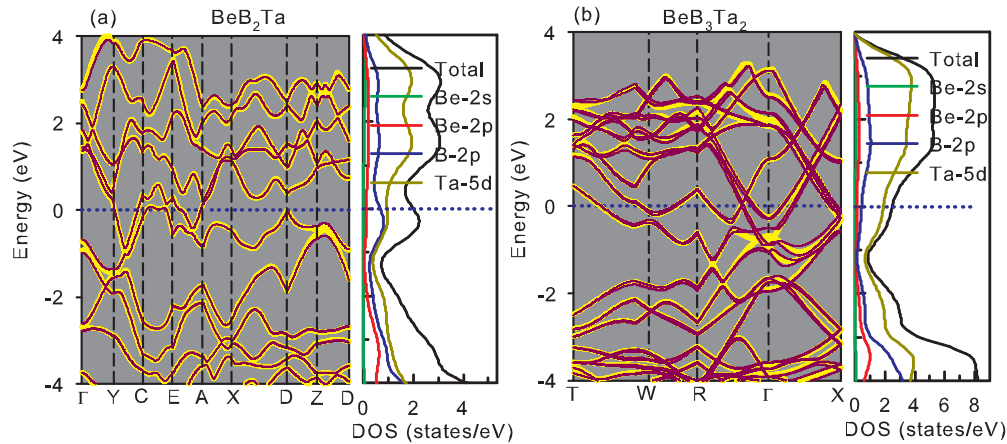
FIG. 4. Electronic band structure, total and projected density of states (states/eV per unit cell) (right-hand panel) of (a) BeB$_2$Ta and (b) BeB$_3$Ta$_2$. The dark pink lines represent energy bands calculated including the spin-orbit coupling effect. The blue dotted line at zero energy represents the Fermi level. The density of states including SOC is not shown here for clarity.

superconductor. Note that spin-orbit coupling effects split both conduction and valence bands. Although Be $2p$ and B $2p$ electrons make contributions to the valence bands, they do not make a significant contribution to the conduction bands, as can be clearly seen from the calculated projected density of states. In contrast to BeBTa$_2$, both Be- and B-rich Be$_2$B$_2$Ta are metals with two bands crossing the Fermi level. One band originates from Ta $5d$ states and another band from the overlap between Be $2p$ and B $2p$ states. Both Be $2p$ and B $2p$ states make significant contributions to the Fermi level. This can be clearly seen from the projected density of states as shown in the left-hand panel of Fig. 5(c). A pseudogap opens along the X-N direction and the Fermi level lies at the top of the pseudogap. This pseudogap arises from Ta $5d$ and Be $2p$ states. From the calculated density of states, it is clear that total density of states at the Fermi level of Be$_2$B$_2$Ta ($\sim$3 states/eV per unit cell) is much higher than that of BeB$_2$Ta ($\sim$2 states/eV per unit cell). The spin-orbit coupling is less significant in Be$_2$B$_2$Ta because Ta is not dominant in this phase. Only a few bands are split by the effect of spin-orbit coupling. Since Ta $5d$ orbitals are hybridized with Be $2p$ and B $2p$ states, this phase may be a potential two-band superconductor. Furthermore, all these bands are highly dispersive. The conduction bands and valence bands overlap significantly indicating the metallic nature. Therefore, these materials would be very useful in different technological applications, for example, as superhard metallic conductors. Further theoretical studies and experimental synthesis of these phases are encouraged to clarify these predictions.

C. Superconductivity

The calculated electronic structure predicts that two phases of Be-B-Ta may be potential superconductors, namely, BeB$_2$Ta and Be$_2$B$_2$Ta. Moreover, MgB$_2$, a simple binary compound, shows high-temperature superconductivity [32], although there are controversies about the superconductivity of TaB$_2$ [33,35]. Therefore, it is interesting to study the electron-phonon interactions in Be-B-Ta containing phases.

The calculated phonon dispersion of BeB$_2$Ta and BeB$_3$Ta$_2$ is shown in the left-hand panel of Fig. 6. The lower-frequency phonons (acoustic phonons) of BeB$_2$Ta arise from Ta atoms, while phonons within the frequency range 300–600 cm^{-1} arise from Be and B. Both Be and B give rise to the higher-frequency optical phonons. It is interesting to note that constituent elements separate the phonon band structure into three regions. The phonon bands of one region do not overlap with the phonon bands of other regions. Two bands within the frequency range $\sim$ 300–600 cm^{-1} correspond to vibrations of B and Be in opposite directions. These three regions induce three dominant peaks in the phonon density of states, as shown in the middle panel of Fig. 6(a). Therefore, the three elements contribute to the phonons almost equally.

Unlike BeB$_2$Ta, the phonon band structure of BeB$_3$Ta$_2$ has four regions [left-hand panel of Fig. 5(b)]. The acoustic phonons arise from Ta atoms, optical phonons within the frequency range 400–600 cm^{-1} from B atoms, and higher-frequency optical phonons (600–900 cm^{-1}) arise from both Be and B. Like BeB$_2$Ta, no phonon bands of one region overlap with the phonon bands of other regions, but the optical phonons of two regions around 550 cm^{-1} overlap with each other when the spin-orbit coupling effect is included (dark pink lines in the dispersion curve). These four regions correspond to the four dominant peaks in the atom projected phonon density of states, as shown in the middle panel of Fig. 6(b). A large gap exists within the frequency range 200–400 cm^{-1}. It is clear that the phonon density of states of BeB$_3$Ta$_2$ is much higher than that of BeB$_2$Ta. Some of the phonon bands of both compounds are split by the spin-orbit effect. However, this effect is much more sensitive in Ta-rich BeB$_3$Ta$_2$ than that in BeB$_2$Ta. Such an effect has been found in many elemental superconductors [74]. No imaginary frequencies in the phonon dispersion ensure the dynamical stability of both compounds.

In the Migdal-Eliashberg formulism [75], the Eliashberg spectral function is written as [54,76]

$$\alpha^2 F(\omega) = \frac{1}{2\pi N(E_F)} \sum_{q\nu} \delta(\omega - \omega_{q\nu}) \frac{\gamma_{q\nu}}{\hbar \omega_{q\nu}}, \qquad (1)$$
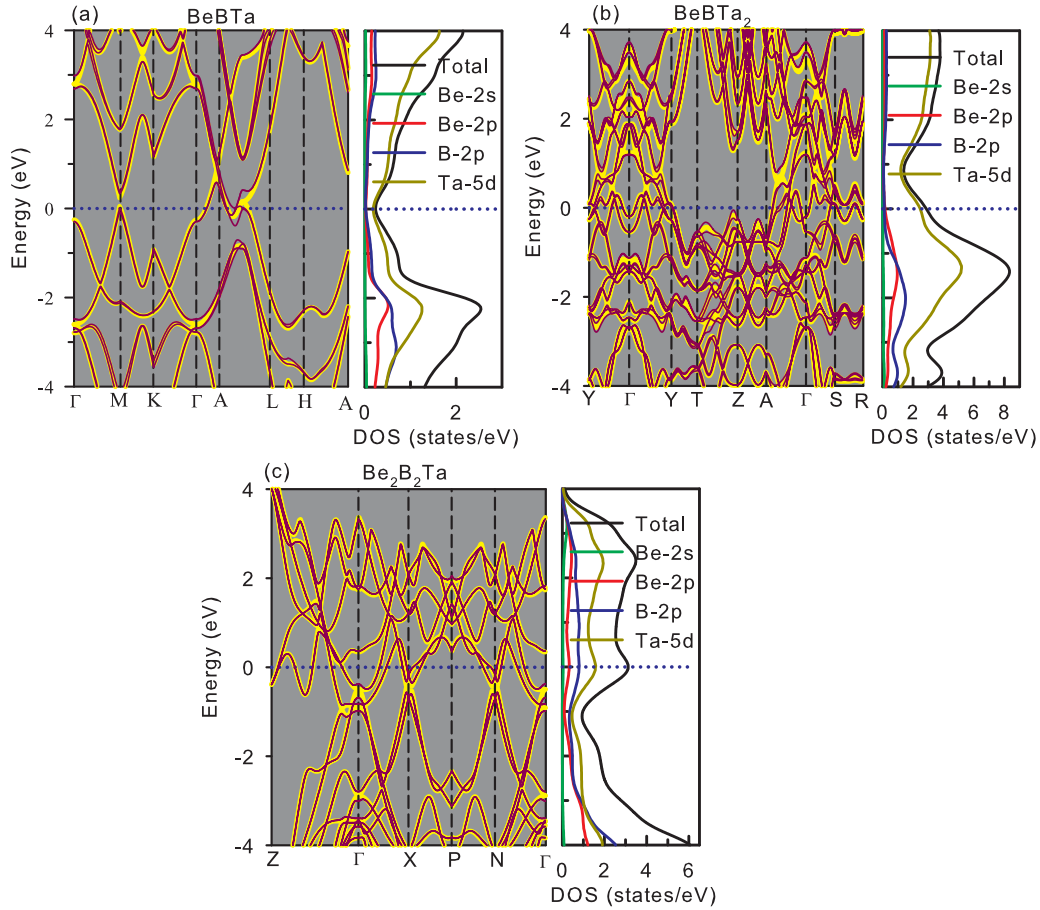
FIG. 5. Electronic band structure, total and projected density of states (right-hand panel) of (a) BeBTa, (b) BeBTa$_2$, and (c) Be$_2$B$_2$Ta. The dark pink lines represent energy bands calculated including the spin-orbit coupling. The blue dotted line at zero energy represents the Fermi level. The density of states including SOC is not shown here for clarity.

where $N(E_F)$ is the density of states at the Fermi level and γ_{qv} is the electron-phonon linewidth for wave vectors q and v.

The calculated Eliashberg spectral function of both compounds is shown in the righthand panels of Fig. 6, with and without the effect of spin-orbit coupling (dark pink line with stars and yellow line, respectively). The Eliashberg function of both compounds has three dominant peaks, although the phonon density of BeB$_3$Ta$_2$ has four dominant peaks. The highest peak in the Eliashberg function (EF) of BeB$_2$Ta arises from the B atoms, while it arises from the Ta atoms in the case of BeB$_3$Ta$_2$. From comparison of the EF with the phonon density of BeB$_2$Ta, it is clear that the electron-phonon (e-ph) interactions are almost equally distributed among all of the phonon modes, but the e-ph interactions in BeB$_3$Ta$_2$ are distributed only among some phonon branches. The higher-frequency optical phonons of BeB$_2$Ta make a significant contribution to the Eliashberg spectral function, but they make a negligible contribution to the EF for the case of BeB$_3$Ta$_2$. Low-frequency acoustic phonons (0–200 cm^{-1}) give rise to ~50% of the total electron-phonon coupling (EPC) in BeB$_3$Ta$_2$ [see the right-hand panel of Fig. 6(b)]. However, only ~25% of the total EPC comes from acoustic phonons in BeB$_2$Ta while optical phonons (from Be and B) provide 75% of the total EPC. This can be further understood from

the mode-dependent EPC calculations. The mode-dependent electron-phonon coupling constant, i.e., the partial contribution of each phonon mode to the total electron-phonon coupling constant, can be written as

$$\lambda_{qv} \equiv \frac{1}{\pi N(E_F)} \frac{\gamma_{qv}}{\omega_{qv}^2}. \qquad (2)$$

By taking the summation of λ_{qv} over v and averaged over the Brillouin zone, the total electron-phonon coupling constant (EPC) λ can be be calculated. The EPC is determined by [54,75]

$$\lambda = 2 \int \frac{\alpha^2 F(\omega)}{\omega} d\omega. \qquad (3)$$

The e-ph coupling distribution is shown in the phonon band structure (left-hand panel of Fig. 6) by the red circles. The radius of the circle is directly proportional to the partial contribution of each phonon to the total e-ph coupling constant (λ). From the figure, the red circles are almost equally distributed among all of the phonon branches of BeB$_2$Ta, but only some phonon branches of BeB$_3$Ta$_2$. The e-ph interactions around the intraband nesting point Γ are present. The strongest e-ph interactions of BeB$_2$Ta are concentrated at Γ-C points, but they are concentered around T-W points in BeB$_3$Ta$_2$. It is
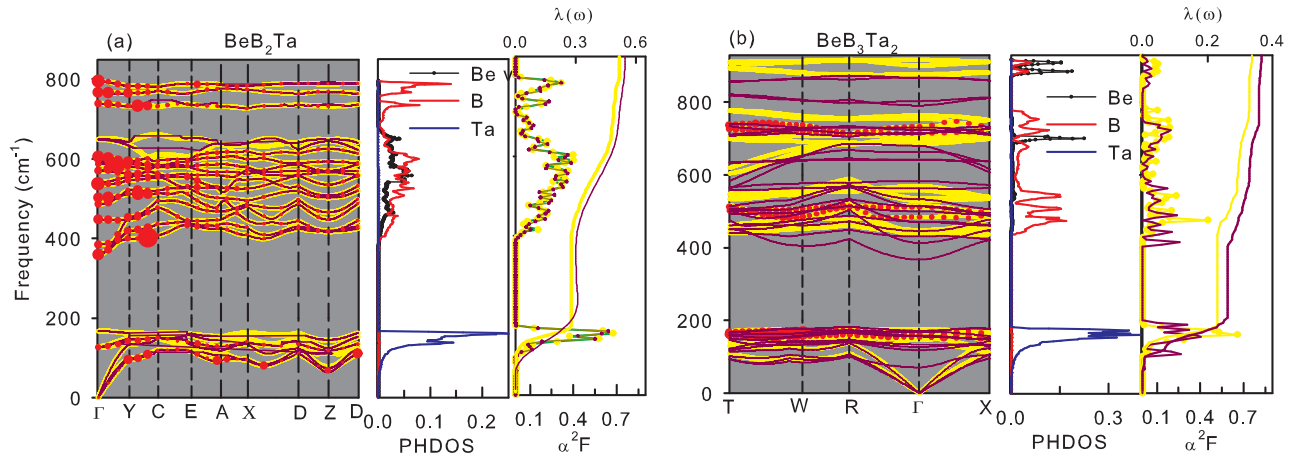
FIG. 6. Electron-phonon related properties of (a) BeB_2Ta and (b) BeB_3Ta_2. The left-hand panel shows the phonon dispersion relations and the middle panel shows atom projected phonon density of states. The dark pink lines in the phonon band structure represent the inclusion of the spin-orbit coupling effect. The phonon density of states, including spin-orbit coupling, is not shown here for clarity. The right-hand panels show the Eliashberg spectral functions and the integrated electron-phonon coupling constant. Similarly, the yellow line represents the Eliashberg spectral function without the spin-orbit coupling effect, while the dark pink line with stars represents the Eliashberg spectral function including the SOC effect. The red circles in the phonon dispersion relations represent mode-dependent electron-phonon coupling constant over the Brillouin zone (see the text).

clear that Ta atoms (acoustic phonons) make the dominant contribution to the total e-ph constant of BeB_3Ta_2, but both Be and B make a significant contribution to the e-ph constant of BeB_2Ta. In a good electron-phonon superconductor, the e-ph coupling is usually concentrated in some phonon modes. Although BeB_3Ta_2 shows this type of distribution, which can be seen from the almost perfect proportionality between phonon density of states and Eliashberg spectral function, the strength of e-ph coupling is very weak (small circle). BeB_2Ta shows a deviation [from perfect proportionality between phonon density of states (PHDOS) and EF], although the strength of the e-ph coupling is strong (large circle).

Unlike BeB_2Ta and BeB_3Ta_2, hexagonal BeBTa and Ta-rich $BeBTa_2$ show little e-ph coupling. The phonon dispersion of BeBTa is similar to BeB_2Ta, in that it can be divided into three regions without any overlapping of phonon bands of each region. However, the acoustic and low-frequency optical phonons make an almost negligible contribution to the e-ph coupling. Only a few higher-frequency optical phonons, around 800 cm^{-1}, are strongly coupled with electrons. These phonons arise from Be and B where Be and B vibrate in the opposite direction. The quite low density of states of B at the Fermi level, i.e., few available electrons of B, can only participate in the e-ph coupling. The corresponding Eliashberg function is quite low and the EF contains only a dominant peak around 800 cm^{-1}. The SOC effect changes the Eliashberg spectral function and shifts the peaks to higher energy. The gross features of the EF are similar to the phonon density of states. Considering the gross features of the phonon dispersions of $BeBTa_2$, it can be seen they are similar to those of BeB_3Ta_2. A large gap exists between the acoustic and optical phonons (from 200 to 500 cm^{-1}), as shown in the left-hand panel of Fig. 7(b). The acoustic phonons arise from the Ta atom (see the atom projected phonon density of states) and provide ~75% of the total e-ph coupling, but the coupling

strength is weak, like BeB_3Ta_2. The optical phonons arising from the B atoms have a small e-ph coupling, as can be seen from the red circles in the phonon dispersion curve. This is because the Ta 5d and B 2p orbitals are strongly hybridized like those in TaB_2. Unlike the former two phases, the e-ph coupling of Be_2B_2Ta is almost equally distributed among all phonon modes. Like BeB_2Ta, the phonon band structure can be divided into three regions. A large gap exists between ~180 and 350 cm^{-1}. Acoustic phonons arising from the Ta atoms make little contribution to the total e-ph coupling. The optical phonons within the frequency range ~350–620 cm^{-1} make the dominant contribution to the total e-ph coupling. These optical phonons arise from both Be and B atoms, where they move back and forth. Another peak in the atom projected phonon density of states of Be_2B_2Ta corresponds to the optical phonons arising from B. Unlike BeB_2Ta, the strongest e-ph couplings [see red circles in the left–hand panel of Fig. 7(c)] are concentrated within the Z-Γ point. The three dominant peaks in the phonon density of states correspond to the three peaks in the Eliashberg spectral function as shown in the right–hand panel of Fig. 7(c). The EF shows almost perfect proportionality with phonon density of states (PHDOS), which is rare in some good e-ph superconductors. It is clear that the SOC effect is less sensitive in this phase as compared to the above-described phases. Only a few phonon bands are split by the SOC effect. The Eliashberg function of Be_2B_2Ta remains almost the same when the SOC effect is included in the calculation, as Be and B make the dominant contribution to the e-ph coupling. By using the calculated Eliashberg spectral function, the logarithmic average phonon frequency (ω_{ln}) can be calculated by peforming the following numerical integration [54,75]:

$$\omega_{ln} = \exp\left[\frac{2}{\lambda}\int\frac{d\omega}{\omega}\alpha^2F(\omega)\ln(\omega)\right]. \quad (4)$$
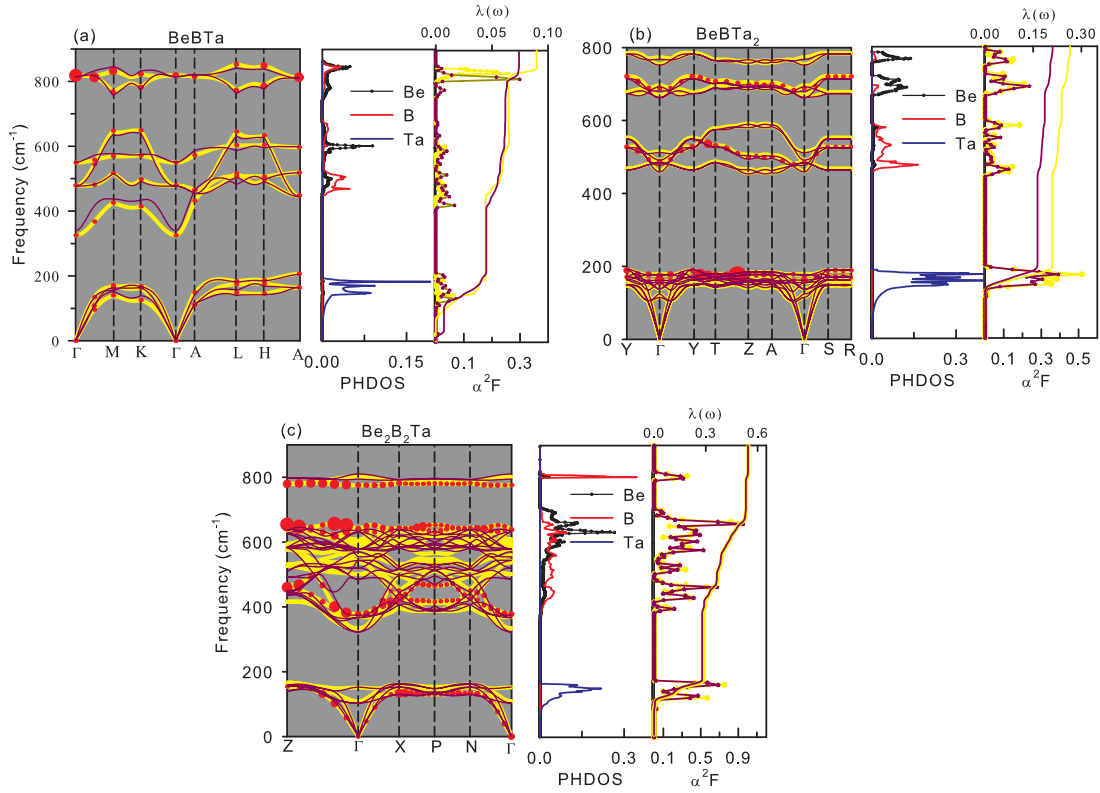
FIG. 7. Electron-phonon related properties of: (a) BeBTa, (b) BeBTa$_2$, and (c) Be$_2$B$_2$Ta. The left-hand panel shows the phonon band structure and the middle panel shows the atom projected phonon density of states. The dark pink line in the phonon band structure represents the inclusion of the spin-orbit coupling. The phonon density of states, including spin-orbit coupling, is not shown here for clarity. The right-hand panels show the Eliashberg spectral functions and the integrated electron-phonon coupling constant. Similarly, the yellow line represents the Eliashberg spectral function without the spin-orbit coupling effect, while the dark pink line with stars represents the Eliashberg spectral function including the SOC effect. The red circles in the phonon dispersions represent mode-dependent electron-phonon coupling constant over the Brillouin zone (see the text).

The calculated total electron-phonon coupling constant and logarithmic average phonon frequency of these phases are listed in Table III. The EPC of BeB$_3$Ta$_2$ and BeBTa$_2$ is very small, while BeBTa has a negligible EPC. According to the electronic structure and *e*-ph properties analysis, these results are not surprising. Only two B-rich phases (BeB$_2$Ta and Be$_2$B$_2$Ta) have a higher EPC as compared to others, as expected. In all phases except BeB$_2$Ta and BeB$_3$Ta$_2$, the SOC effect reduces the EPC constant slightly. The logarithmic average phonon frequency of all compounds, except

BeB$_2$Ta and BeB$_3$Ta$_2$, is increased when the SOC effect is included.

Using the calculated EPC and logarithmic average phonon frequency, the superconducting transition temperature can be calculated by using the Allen-Dynes equation [54,76],

$$T_c = \frac{\omega_{\ln}}{1.2} \exp\left[\frac{-1.04(1+\lambda)}{\lambda(1-0.62\mu^*) - \mu^*}\right], \qquad (5)$$

where μ^* stands for Coulomb pseudopotential constant and its value ranges between 0.1 and 0.15 [77,78]. Here, the most widely accepted value, 0.1, of μ^* has been used to evaluate the superconducting transition temperature.

From Table III, it is clear that the superconductivity is absent in the Ta-rich (or equivalent) phases, BeBTa$_2$ and BeBTa. The BeB$_3$Ta$_2$ structure may not be a superconductor since the calculated T_c is too small. These results are consistent with the electronic structure calculations. Only BeB$_2$Ta and Be$_2$B$_2$Ta are superconductors. The obtained T_c of these two phases is slightly increased due to the inclusion of the SOC effect, as the total EPC and logarithmic average phonon frequency are changed. Therefore, Be-B brings the superconductivity in these two phases of Be-B-Ta (see the Supplemental Material [79] for further discussion). The above results predict that any combination of B-rich with an electron-rich transition metal may be a potential superconductor if the hybridization

TABLE III. The calculated total EPC (λ), logarithmic average phonon frequency ($\omega_{\ln}$), and superconducting transition temperature of all stable phases under ambient conditions. Inside the brackets, the calculated value of the parameter including the SOC effect is presented. In all cases, the value 0.1 of μ^* is used.

Compound	λ	$\omega_{\ln}$ (K)	T_c (K)
BeB$_2$Ta	0.519 (0.526)	388.72 (393.2)	5.45 (5.8)
BeB$_3$Ta$_2$	0.338 (0.366)	343.8 (303. 8)	0.47 (0.73)
BeBTa$_2$	0.265 (0.211)	307.6 (314.8)	0.04 ($\sim$0)
BeBTa	0.081 (0.076)	411.9 (316.9)	$\sim$0 ($\sim$0)
Be$_2$B$_2$Ta	0.546 (0.545)	390.1 (399.0)	6.6 (6.7)

between the B $2p$ and electron-rich element d orbitals is disturbed by another $2s$ element.

The predicted five compounds show useful properties, such as higher hardness (26–37 GPa) as compared to the existing binary compounds (26–30 GPa, for example, TaB [31]) and higher superconducting transition temperature (6–7 K) as compared to the existing binary compounds ($\sim$1 K, for example, BeB$_{2.75}$ [9]). Therefore, these ternary compounds will bring a significant advance to the existing binary compounds.

IV. CONCLUSIONS

In summary, stable crystal structures containing Be-B-Ta at ambient conditions have been predicted by using variable-composition evolutionary crystal structure search calculations based on first-principles calculations. The structural stability, mechanical, electronic, and superconducting properties of the stable phases have been discussed. The predicted five compounds BeB$_2$Ta, BeB$_3$Ta$_2$, BeBTa, BeBTa$_2$, and Be$_2$B$_2$Ta have been found to be highly dense and very hard materials. They may be potential candidates for superhard materials in

different technological applications. All these ternary stable compounds are metallic and spin-orbit coupling (SOC) effects split some energy bands arising from Ta $5d$. In BeB$_3$Ta$_2$, BeBTa, and BeBTa$_2$, Ta $5d$ and B $2p$ orbitals are strongly hybridized, while Be $2p$ orbitals make a significant contribution to the hybridization in BeB$_2$Ta and Be$_2$B$_2$Ta. Thus, two of the stable phases (BeB$_2$Ta and Be$_2$B$_2$Ta) have been found to be superconductors within Migdal-Eliashberg theory. Therefore, any stable combination of B-rich with an electron-rich transition metal (for example, La, Hf, etc.) may be potential superconductors if the hybridization between B $2p$ and electron-rich element d orbitals is disturbed by another $2s$ element (such as Mg, Ca, Sr, etc.). The calculated critical temperature, including SOC effects, is 6 and 7 K for BeB$_2$Ta and Be$_2$B$_2$Ta, respectively. Because of their energetic and dynamic stability, these compounds might be favorable to synthesize in the laboratory. In the same way, we can predict several hundred potential compounds from the combination of I$_A$-II$_A$, transition metals (III$_B$-II$_B$), and metalloids (III$_A$). These will guide researchers to predict practically useful compounds containing same series of elements.

[1] K. Kádas, L. Vitos, B. Johansson, and J. Kollár, Phys. Rev. B **75**, 35132 (2007).

[2] K. Kádas, L. Vitos, R. Ahuja, B. Johansson, and J. Kollar, Phys. Rev. B **76**, 235109 (2007).

[3] A. Allouche, M. Oberkofler, M. Reinelt, and C. Linsmeier, J. Phys. Chem. C **114**, 3588 (2010).

[4] G. Robert, P. Legrand, and S. Bernard, Phys. Rev. B **82**, 104118 (2010).

[5] Y. Xia, Q. Li, and Y. Ma, Comput. Mater. Sci. **49**, S76 (2010).

[6] Y. Wang and Y. Xiong, Mater. Sci. Eng. A **280**, 124 (2000).

[7] I. R. Shein and A. L. Ivanovskii, Phys. Status Solidi **227**, R1 (2001).

[8] H. J. Becher and A. Schäfer, Z. Anorg. Allg. Chem. **318**, 304 (1962).

[9] D. P. Young, R. G. Goodrich, P. W. Adams, J. Y. Chan, F. R. Fronczek, F. Drymiotis, and L. L. Henry, Phys. Rev. B **65**, 180518(R) (2002).

[10] C. Fan, Y. Jin, J. Li, and X. Dong, Sci. Rep. **4**, 6993 (2014).

[11] A. Hermann, N. W. Ashcroft, and R. Hoffmann, Chem. - Eur. J. **19**, 4184 (2013).

[12] A. Hermann, N. W. Ashcroft, and R. Hoffmann, Inorg. Chem. **51**, 9066 (2012).

[13] M. C. Nguyen, X. Zhao, C.-Z. Wang, and K.-M. Ho, RSC Adv. **4**, 15061 (2014).

[14] F. Occelli, P. Loubeyre, and R. LeToullec, Nat. Mater. **2**, 151 (2003).

[15] Z. Pan, H. Sun, Y. Zhang, and C. Chen, Phys. Rev. Lett. **102**, 55503 (2009).

[16] V. L. Solozhenko, S. N. Dub, and N. V Novikov, Diamond Relat. Mater. **10**, 2228 (2001).

[17] J. B. Levine, S. H. Tolbert, and R. B. Kaner, Adv. Funct. Mater. **19**, 3519 (2009).

[18] Z. Zhao, M. Wang, L. Cui, J. He, D. Yu, and Y. Tian, J. Phys. Chem. C **114**, 9961 (2010).

[19] H.-Y. Chung, M. B. Weinberger, J.-M. Yang, S. H. Tolbert, and R. B. Kaner, Appl. Phys. Lett. **92**, 261904 (2008).

[20] X. Hao, Y. Xu, Z. Wu, D. Zhou, X. Liu, X. Cao, and J. Meng, Phys. Rev. B **74**, 224112 (2006).

[21] R. W. Cumberland, M. B. Weinberger, J. J. Gilman, S. M. Clark, S. H. Tolbert, and R. B. Kaner, J. Am. Chem. Soc. **127**, 7264 (2005).

[22] A. L. Ivanovskii, Prog. Mater. Sci. **57**, 184 (2012).

[23] H.-Y. Chung, M. B. Weinberger, J. B. Levine, A. Kavner, J.-M. Yang, S. H. Tolbert, and R. B. Kaner, Science **316**, 436 (2007).

[24] Z.-J. Wu, E.-J. Zhao, H.-P. Xiang, X.-F. Hao, X.-J. Liu, and J. Meng, Phys. Rev. B **76**, 54115 (2007).

[25] J. S. Tse, D. D. Klug, Z. Uehara, Z. Q. Li, J. Haines, and J. M. Leger, Phys. Rev. B **61**, 10029 (2000).

[26] R. F. Zhang, D. Legut, Z. J. Lin, Y. S. Zhao, H. K. Mao, and S. Veprek, Phys. Rev. Lett. **108**, 255502 (2012).

[27] H. Gou, Z. Li, H. Niu, F. Gao, J. Zhang, R. C. Ewing, and J. Lian, Appl. Phys. Lett. **100**, 111907 (2012).

[28] S. Okada, K. Kudou, I. Higashi, and T. Lundström, J. Cryst. Growth **128**, 1120 (1993).

[29] S. Motojima, K. Kito, and K. Sugiyama, J. Nucl. Mater. **105**, 262 (1982).

[30] S. Otani, M. M. Korsukova, and T. Mitsuhashi, J. Cryst. Growth **194**, 430 (1998).

[31] H.-H. Chen, Y. Bi, Y. Cheng, G. Ji, and L. Cai, J. Phys. Chem. Solids **73**, 1197 (2012).

[32] J. Nagamatsu, N. Nakagawa, T. Muranaka, Y. Zenitani, and J. Akimitsu, Nature **410**, 63 (2001).

[33] D. Kaczorowski, A. J. Zaleski, O. J. Żogał, and J. Klamut, arXiv:cond-mat/0103571v2 [cond-mat.supr.con] (2001).

[34] D. Kaczorowski, J. Klamut, and A. J. Zaleski, arXiv:cond-mat/0104479v1 [cond-mat.supr.con] (2001).

[35] H. Rosner, W. E. Pickett, S.-L. Drechsler, A. Handstein, G. Behr, G. Fuchs, K. Nenkov, K.-H. Müller, and H. Eschrig, Phys. Rev. B **64**, 144516 (2001).

[36] V. A. Gasparov, N. S. Sidorov, I. I. Zver'Kova, and M. P. Kulakov, J. Exp. Theor. Phys. Lett. **73**, 532 (2001).

[37] C. W. Glass, A. R. Oganov, and N. Hansen, Comput. Phys. Commun. **175**, 713 (2006).

[38] A. R. Oganov and C. W. Glass, J. Chem. Phys. **124**, 244704 (2006).

[39] A. R. Oganov and C. W. Glass, J. Phys.: Condens. Matter **20**, 064210 (2008).

[40] A. O. Lyakhov, A. R. Oganov, H. T. Stokes, and Q. Zhu, Comput. Phys. Commun. **184**, 1172 (2013).

[41] Y. Xie, A. R. Oganov, and Y. Ma, Phys. Rev. Lett. **104**, 177005 (2010).

[42] Y. Ma, M. Eremets, A. R. Oganov, Y. Xie, I. Trojan, S. Medvedev, A. O. Lyakhov, M. Valle, and V. Prakapenka, Nature **458**, 182 (2009).

[43] Y. Ma, A. R. Oganov, and Y. Xie, Phys. Rev. B **78**, 14102 (2008).

[44] A. R. Oganov, J. Chen, C. Gatti, Y. Ma, Y. Ma, C. W. Glass, Z. Liu, T. Yu, O. O. Kurakevych, and V. L. Solozhenko, Nature **457**, 863 (2009).

[45] P. Giannozzi, S. Baroni, N. Bonini, M. Calandra, R. Car, C. Cavazzoni, D. Ceresoli, G. L. Chiarotti, M. Cococcioni, I. Dabo *et al.*, J. Phys.: Condens. Matter **21**, 395502 (2009).

[46] J. P. Perdew, K. Burke, and M. Ernzerhof, Phys. Rev. Lett. **77**, 3865 (1996).

[47] J. P. Perdew, A. Ruzsinszky, G. I. Csonka, O. A. Vydrov, G. E. Scuseria, L. A. Constantin, X. Zhou, and K. Burke, Phys. Rev. Lett. **100**, 136406 (2008).

[48] D. Vanderbilt, Phys. Rev. B **41**, 7892 (1990).

[49] D. Raczkowski, A. Canning, and L. W. Wang, Phys. Rev. B **64**, 121101(R) (2001).

[50] S. J. Clark, M. D. Segall, C. J. Pickard, P. J. Hasnip, M. I. J. Probert, K. Refson, and M. C. Payne, Z. Krist. Mater. **220**, 567 (2005).

[51] R. Hill, Proc. Phys. Soc., London, Sect. A **65**, 349 (1952).

[52] X. Q. Chen, H. Niu, D. Li, and Y. Li, Intermetallics **19**, 1275 (2011).

[53] N. Marzari, D. Vanderbilt, A. De Vita, and M. C. Payne, Phys. Rev. Lett. **82**, 3296 (1999).

[54] P. B. Allen and R. C. Dynes, Phys. Rev. B **12**, 905 (1975).

[55] A. Dal Corso, Phys. Rev. B **76**, 54308 (2007).

[56] R. L. Falge Jr., Phys. Lett. A **24**, 579 (1967).

[57] K. J. H. Mackay and N. A. Hill, J. Nucl. Mater. **8**, 263 (1963).

[58] B. F. Decker and J. S. Kasper, Acta Crystallogr. **12**, 503 (1959).

[59] H. Cynn and C.-S. Yoo, Phys. Rev. B **59**, 8526 (1999).

[60] A. G. Van Der Geest and A. N. Kolmogorov, CALPHAD: Comput. Coupling Phase Diagrams Thermochem. **46**, 184 (2014).

[61] B. Chu, D. Li, K. Bao, F. Tian, D. Duan, X. Sha, P. Hou, Y. Liu, H. Zhang, B. Liu *et al.*, J. Alloys Compd. **617**, 660 (2014).

[62] B. Predel, in *Landolt-Bornstein—Group IV Physical Chemistry, Phase Equilibria, Crystallographic and Thermodynamic Data of Binary Alloys*, edited by B. Predel (Springer, Berlin, Heidelberg, 1992), p. 1.

[63] A. R. Oganov, Y. Ma, C. W. Glass, and M. Valle, Psi-k Newsl. **84**, 142 (2007).

[64] T. F. T. Cerqueira, S. Lin, M. Amsler, S. Goedecker, S. Botti, and M. A. L. Marques, Chem. Mater. **27**, 4562 (2015).

[65] M. N. Ali, F. von Rohr, C. Campana, A. Schilling, and R. J. Cava, Mater. Res. Bull. **70**, 673 (2015).

[66] G. Wenski and A. Mewis, Z. Krist. Mater. **176**, 125 (1986).

[67] W. Jeitschko and M. H. Gerss, J. Less-Common Met. **116**, 147 (1986).

[68] G. Just and P. Paufler, J. Alloys Compd. **232**, 1 (1996).

[69] F. Mouhat and F.-X. Coudert, Phys. Rev. B **90**, 224104 (2014).

[70] S. F. Pugh, London, Edinburgh, Dublin Philos. Mag. J. Sci. **45**, 823 (1954).

[71] M. K. Y. Chan and G. Ceder, Phys. Rev. Lett. **105**, 196403 (2010).

[72] D. Koller, F. Tran, and P. Blaha, Phys. Rev. B **83**, 195134 (2011).

[73] N. P. Armitage, E. J. Mele, and A. Vishwanath, Rev. Mod. Phys. **90**, 15001 (2018).

[74] R. Heid, K.-P. Bohnen, I. Y. Sklyadneva, and E. V. Chulkov, Phys. Rev. B **81**, 174527 (2010).

[75] G. M. Eliashberg, Zh. Eksp. Teor. Fiz. **38**, 966 (1960) [JETP **11**, 696 (1960)].

[76] P. B. Allen, Phys. Rev. B **6**, 2577 (1972).

[77] C. F. Richardson and N. W. Ashcroft, Phys. Rev. Lett. **78**, 118 (1997).

[78] K.-H. Lee, K.-J. Chang, and M. L. Cohen, Phys. Rev. B **52**, 1425 (1995).

[79] See Supplemental Material at http://link.aps.org/supplemental/10.1103/PhysRevMaterials.3.084804 for optimized fractional atomic coordinates, Fermi velocity, and Fermi surface.